



# Investigations into nanostructured ceria–zirconia catalysts for soot combustion



Marco Piumetti, Samir Bensaid, Nunzio Russo, Debora Fino\*

Department of Applied Science and Technology, Politecnico di Torino, Corso Duca degli Abruzzi 24, 10129 Turin, Italy

## ARTICLE INFO

### Article history:

Received 1 April 2015

Received in revised form 3 June 2015

Accepted 11 June 2015

Available online 16 June 2015

### Keywords:

Ceria

Ceria–zirconia

Soot oxidation

Nanostructured ceria

Nano-polyhedra

## ABSTRACT

A set of nanostructured ceria–zirconia catalysts with different Zr-contents and structural features has been prepared to study the effect of both the Zr-amount and its surface-dependent activity towards soot combustion under different experimental conditions (namely in “loose” and “tight” soot-catalyst contact). A ceria–zirconia sample has been synthesized by means of solution combustion synthesis (SCS) for comparison purposes. The physico-chemical properties of the catalysts have been investigated using complementary techniques.

The best catalytic performances have been achieved for the  $\text{Ce}_{0.9}\text{Zr}_{0.1}\text{O}_2$ -NP catalyst (where NP means nano-polyhedra and 0.9 indicates the atomic ratio of Ce/Ce + Zr), due to the higher mobility of the lattice oxygen within the solid, and its easier reducibility, compared to high-surface area catalysts with the same Ce/Zr ratio. Moreover, better activities, in terms of soot conversions, have been reached for  $\text{Ce}_{0.9}\text{Zr}_{0.1}\text{O}_2$ -NP, than similar nano-polyhedra with higher Zr-amounts (denoted as  $\text{Ce}_x\text{Zr}_{1-x}\text{O}_2$ -NP, where  $x = 0.8$  or  $0.7$ ). The substitution of some  $\text{Ce}^{4+}$  for  $\text{Zr}^{4+}$  ions favors the formation of defects (i.e., oxygen vacancies) in the ceria lattice, thus inducing a distortion of the oxygen sublattice. However, the amount of redox Ce species decreases as the Zr-content increases. It therefore seems that the incorporation of  $\text{Zr}^{4+}$  into the ceria lattice does not have a direct beneficial effect on the oxidation activity for catalysts calcined at low/mild temperatures, since it decreases the population of surface redox-active centers, which depend directly on the surface density of the  $\text{Ce}^{3+}$ – $\text{Ce}^{4+}$  species. On the other hand, lower soot conversion values have been reached for both mesoporous ( $\text{Ce}_{0.9}\text{Zr}_{0.1}\text{O}_2$ -M) and microporous ( $50\text{-Ce}_{0.9}\text{Zr}_{0.1}\text{O}_2$ -NP/FAU) samples with the same Ce/Zr ratio. Moreover, the comparative catalyst ( $\text{Ce}_{0.9}\text{Zr}_{0.1}\text{O}_2$ -SCS) exhibited worse activities than the porous materials, thus confirming the key role of the textural properties for this oxidation reaction.

© 2015 Elsevier B.V. All rights reserved.

## 1. Introduction

Over the last few years, several exhaust gas after treatment technologies have been proposed to limit Diesel engine-out emissions. The latter are sources of the main outdoor air pollutants, including volatile organic compounds (VOCs), nitrogen oxides ( $\text{NO}_x$ ) and particulate matter (PM), which is largely comprised of solid carbon (soot) and unburned carbonaceous compounds [1–3]. Soot, in particular, is a major constituent of air pollution, and is associated with respiratory and cardiovascular diseases as well as skin cell alterations [4]. Therefore, recent legislation has introduced more stringent PM limits for vehicles (e.g., 0.005 g/km for PM from passenger cars in Europe since 2009) and has imposed the use of catalytic technologies to satisfy the required standards [1,3].

Among the different alternatives, the entrapment of particulate from exhaust gases by Diesel particulate filters (DPFs) has received much interest in recent years [5–10]. The soot that forms Diesel exhaust particulate can be burnt off above 600 °C, whereas, typical engine exhaust temperatures fall within the 200–500 °C range [8,9]. Consequently, oxidation catalysts are required to improve the soot combustion activity within the DPFs.

According to the literature [1,3,4], ceria-based materials are among the most effective catalysts for soot combustion under either an  $\text{O}_2$  or an  $\text{NO}_x/\text{O}_2$  atmosphere, since they exhibit excellent redox properties of the  $\text{Ce}^{3+}$ – $\text{Ce}^{4+}$  couple and can exchange oxygen with the gas phase. In fact, ceria alone, or doped with metals (e.g., Zr, Fe, K, La, Pr, Sm, Tb, Cu, Mn, and Mo) is able to show promising soot combustion activities [4,10–15]. The incorporation of isoalent non-reducible elements, such as  $\text{Zr}^{4+}$  ions, into a ceria lattice (Zr-content in the 20–30 mol.%) has a beneficial effect on the physico-chemical and catalytic properties of ceria, improving its thermal stability, oxygen storage capacity (OSC), oxygen mobil-

\* Corresponding author. Fax: +39 11 0904699.  
E-mail address: [debora.fino@polito.it](mailto:debora.fino@polito.it) (D. Fino).

ity in the framework, and so on [4]. Moreover, the substitution of  $\text{Ce}^{4+}$  ions with  $\text{Zr}^{4+}$  favors the formation of structural defects (e.g., terraces, ledges, kinks, and oxygen vacancies) with surface atoms having different coordination environments (namely coordination numbers, CN) [16]. It should be noted that defect sites and oxygen vacancies are among the most desirable active sites for oxidation catalysts [17,18]. In agreement with the Volkenshtein Electronic Theory [19], the presence of structural defects, associated with oxygen vacancies, in fact modifies the Fermi Energy level, thus, favoring oxidation reactions [20]. Therefore, it can be expected that ceria–zirconia catalysts will exhibit superior soot oxidation activities than pure ceria [4,10–15].

However, it should be pointed out that the feasibility of the soot combustion mechanism depends to a great extent on the soot–catalyst contact points, and hence it is necessary to maximize the interaction between the soot particles and the catalyst surface [11,14].

Over the last few decades, many studies related to  $\text{CeO}_2$  nanoparticles have shown that surface atoms with a lower CN usually exhibit higher chemical reactivity, and are therefore, the preferred active centers for catalytic reactions [1,10]. Nanomaterials are notable because of their small featured size, which endows them with structure-dependent properties, due to the high surface-to-volume ratio (the small size maximizes the surface active sites) and unique electronic features (=discrete behavior) [18–20].

However, the reactivity of nanoparticles depends not only on their size, but also on the crystal surfaces and thus, on the exposed planes [21,22]. Nanostructured  $\text{CeO}_2$ -based materials, having specific surface planes, have shown promising catalytic activities for many reactions, including soot combustion [10,23–31]. Small ceria particles, with an abundance of (100) and (110) planes, are usually more active than larger  $\text{CeO}_2$ -particles with preferred exposure of the (111) planes [32–34]. A study by Zhang et al. [35] on ceria nanocubes, that exposed six (100) surfaces, revealed greater oxygen storage which can be attributed to the ease of O extraction from those surfaces. On the other hand, since the overall oxidation activity depends on the surface area available from the solid catalyst, it is necessary to maximize the dispersion of the nanoparticles using high-surface-area supports, such as zeolites [1,9].

In the present work, a set of ceria–zirconia catalysts, with different Zr-contents and structural properties, has been prepared to investigate the effect of both Zr-loading and the surface-dependency activity of catalysts towards the soot oxidation reaction. The physico-chemical properties of the prepared materials have also been studied using complementary techniques.

## 2. Experimental

### 2.1. Preparation of the samples

Three nanostructured ceria–zirconia catalysts (denoted hereafter as  $\text{Ce}_x\text{Zr}_{1-x}\text{O}_2$ -NP where NP means nano-polyhedra, whereas  $x=0.9, 0.8$ , or  $0.7$  indicates the atomic ratio of  $\text{Ce}/(\text{Ce}+\text{Zr})$  have been synthesized by means of a hydrothermal procedure. During a typical synthesis, appropriate amounts of  $\text{Ce}(\text{NO}_3)_3 \cdot 6\text{H}_2\text{O}$  and  $\text{ZrOCl}_2 \cdot 8\text{H}_2\text{O}$  (Sigma–Aldrich) were dissolved in 30 mL of distilled water (“solution I”). Zirconyl chloride was chosen as Zr precursor, since it is a proper candidate for the synthesis of the ceria–zirconia nanostructures by hydrothermal procedure [36]. Meanwhile, “solution II” was prepared by adding NaOH (24 g) to distilled water (35 mL). The two solutions were then mixed together and stirred at room temperature for 1 h, which resulted in the formation of a milky slurry. The final mixture was transferred to a Teflon autoclave (150 mL) which was 70% filled with deionized water. The mixture was then aged at  $110^\circ\text{C}$  for 24 h. The fresh precipitates were sepa-

rated by centrifugation, washed with deionized water and ethanol several times and dried at  $90^\circ\text{C}$  overnight. The powders were calcined at  $550^\circ\text{C}$  for 4 h.

An ordered mesoporous sample (denoted as  $\text{Ce}_{0.9}\text{Zr}_{0.1}\text{O}_2$ -M) was prepared by means of the following procedure: 0.35 g of  $\text{Ce}(\text{NO}_3)_3 \cdot 6\text{H}_2\text{O}$  and 0.05 g of  $\text{ZrO}(\text{NO}_3)_2$  (Sigma–Aldrich) were dissolved in 5 mL of absolute ethanol. Then, 0.15 g of KIT-6 (mesoporous silica molecular sieve by ACS materials) was added to this solution and heated at  $60^\circ\text{C}$  under vigorous stirring for 30 min. After the ethanol had evaporated, the cerium precursor/silica composite was calcined at  $350^\circ\text{C}$  for 4 h. The impregnation step was repeated in order to achieve higher loadings. The powder was dried at  $110^\circ\text{C}$  overnight and calcined at  $550^\circ\text{C}$  for 6 h. The silica template was then removed and treated three times with a 2 M NaOH solution at  $50^\circ\text{C}$  (10 min each time). The powder was washed with deionized water. Finally, the obtained product was dried at  $90^\circ\text{C}$  overnight.

The 25-, 50-, and 75- $\text{Ce}_{0.9}\text{Zr}_{0.1}\text{O}_2$ -NP/FAU catalysts ( $\text{Ce}_{0.9}\text{Zr}_{0.1}\text{O}_2$ -NP contents = 25, 50, and 75 wt.%, respectively) were prepared by adding appropriate amounts of  $\text{Ce}_{0.9}\text{Zr}_{0.1}\text{O}_2$ -NP to the Faujasite-type zeolite (Sigma–Aldrich), and placing the mixtures in a rotary evaporator at  $60^\circ\text{C}$  to evacuate the water. The obtained solids were then dried at  $90^\circ\text{C}$  overnight. A ceria–zirconia sample (denoted as  $\text{Ce}_{0.9}\text{Zr}_{0.1}\text{O}_2$ -SCS) was prepared by means of solution combustion synthesis (SCS) for comparison purposes [37]. In short, a homogeneous aqueous solution of  $\text{Ce}(\text{NO}_3)_3 \cdot 6\text{H}_2\text{O}$  (1.9 g),  $\text{ZrO}(\text{NO}_3)_2$  (0.11 g) and urea (0.8 g), prepared at room temperature, was placed in an oven at  $600^\circ\text{C}$  for 20 min. The resultant powder was washed with deionized water to remove impurities and then dried at  $90^\circ\text{C}$  overnight.

### 2.2. Characterization of the catalysts

The powder X-ray diffraction patterns have been collected on a X'Pert Philips PW3040 diffractometer using  $\text{Cu K}\alpha$  radiation ( $2\theta$  range =  $20$ – $70^\circ$ ; step =  $0.05^\circ$   $2\theta$ ; time per step =  $0.2$  s). The diffraction peaks were indexed according to the Powder Data File database (PDF 2000, International Center of Diffraction Data, Pennsylvania). The average size of the crystallites was obtained using the Scherrer formula,  $D = 0.9\lambda/b\cos\theta$ , where  $\lambda$  is the wavelength of the  $\text{Cu K}\alpha$  radiation,  $b$  is the full width at half maximum (in radians),  $0.9$  is the shape factor for spherical particles, and  $\theta$  is the angle of the diffraction peaks.

The Specific Surface Area ( $S_{\text{BET}}$ ), total pore volume ( $V_p$ ), and average pore diameter ( $D_p$ ) were measured by means of  $\text{N}_2$  physisorption at  $-196^\circ\text{C}$  (Micrometrics ASAP 2020) on samples previously outgassed at  $200^\circ\text{C}$  for 4 h to remove water and other atmospheric contaminants. The specific surface area of the samples was calculated using the BET method, whereas the pore diameters were evaluated by applying the Barrett–Joyner–Halenda (BJH) algorithm to the isotherm desorption branch.

Sample morphology was studied by using a field emission scanning electron microscope (FESEM Zeiss MERLIN, Gemini-II column) and Transmission Electron Microscopy (TEM, Jeol JEM 3010 operating at 200 kV). The Ce/Zr-content in the samples was determined through EDS analysis (Oxford X-ACT): 5 different spots with a 10–50 nm diameter were selected in representative zones of the sample, and the average Ce/Zr-content was then calculated.

$\text{H}_2$ -TPR analysis was carried out in a Thermoquest TPD/R/O 1100 analyzer equipped with a thermal conductivity (TCD) detector: a 50 mg sample was placed in a quartz tube, then put in contact with reducing flowing gas (4.95% molar  $\text{H}_2$  in Ar,  $40\text{ cm}^3\text{ min}^{-1}$ ) and heated in the  $25$ – $900^\circ\text{C}$  temperature range (heating rate:  $5^\circ\text{C min}^{-1}$ ), while  $\text{H}_2$  consumption was recorded using a thermal conductivity detector (TCD).

**Table 1**Textural properties of the samples, as derived from both XRD analysis and N<sub>2</sub> isotherms at –196 °C.

Catalyst	Crystal size <sup>a</sup> (nm)	S <sub>BET</sub> (m <sup>2</sup> g <sup>–1</sup> )	V <sub>p</sub> <sup>b</sup> (cm <sup>3</sup> g <sup>–1</sup> )	D <sub>p</sub> <sup>c</sup> (nm)
Ce <sub>0.9</sub> Zr <sub>0.1</sub> O <sub>2</sub> –NP	17	2	0.01	–
Ce <sub>0.8</sub> Zr <sub>0.2</sub> O <sub>2</sub> –NP	18	2	0.01	–
Ce <sub>0.7</sub> Zr <sub>0.3</sub> O <sub>2</sub> –NP	16	3	0.01	–
Ce <sub>0.9</sub> Zr <sub>0.1</sub> O <sub>2</sub> –M	23	121	0.24	6
Ce <sub>0.9</sub> Zr <sub>0.1</sub> O <sub>2</sub> –SCS	28	20	0.03	6
25–Ce <sub>0.9</sub> Zr <sub>0.1</sub> O <sub>2</sub> –NP/FAU	17	546	0.26	0.5
50–Ce <sub>0.9</sub> Zr <sub>0.1</sub> O <sub>2</sub> –NP/FAU	17	521	0.25	0.5
75–Ce <sub>0.9</sub> Zr <sub>0.1</sub> O <sub>2</sub> –NP/FAU	17	236	0.18	0.5

<sup>a</sup> Calculated applying the Scherrer formula.<sup>b</sup> V<sub>p</sub> = total pore volume.<sup>c</sup> D<sub>p</sub> = pore diameter calculated according to the BJH method.

Raman spectra were recorded on a micro-Raman system (Renishaw ViaReflex) equipped with an Ar–Kr laser, by exciting at 514.5 nm.

X-ray photoelectron spectroscopy measurements were obtained on XPS PHI 5000 Versa probe apparatus using a band-pass energy of 187.85 eV, a 45° take off angle and a 100.0 μm diameter X-ray spot size. Curve-fits were performed by means of Multipack 9.0 software.

### 2.3. Catalytic activity tests

The soot oxidation activity of the prepared catalysts has been measured by means of temperature programmed oxidation (TPO), which was carried out in a fixed-bed micro-reactor (a quartz U-tube, with an inner diameter of 4 mm, heated by an electric oven). The temperature was measured by means of a thermocouple placed close to the middle of the catalytic bed. An N<sub>2</sub> flow, containing 10% of O<sub>2</sub>, was fed at a constant rate of 100 cm<sup>3</sup> min<sup>–1</sup> to the fixed bed, which was constituted by 50 mg of a carbon mixture (Printex-U) and powdered catalyst (=45 mg of catalyst and 5 mg of soot) mixed with 150 mg of inert silica. Two types of soot-catalyst contact conditions were considered:

- “Loose” contact: the soot-catalyst mixture was prepared by gently shaking it with a spatula for 1 min. This procedure was sufficient to homogenize the mixture, but still allowed the two solid phases to be put in loose contact.
- “Tight” contact: the soot-catalyst mixture was obtained through ball milling (250 rpm for 10 min) to reach an intimate contact between the soot and catalyst. This method maximizes the soot-catalyst interaction and, although it is less representative for the real conditions that occur in a catalytic trap, it is able to better discriminate the activity of the different catalysts.

The reaction temperature was controlled by means of a PID-regulated oven and varied from 100 to 700 °C at a 5 °C min<sup>–1</sup> rate. The CO/CO<sub>2</sub> concentration in the outlet gas was measured via NDIR analyzers (ABB). Temperatures corresponding to 10%, 50%, and 90% soot conversion (denoted as T<sub>10%</sub>, T<sub>50%</sub>, T<sub>90%</sub>, respectively) were taken as indices of the catalytic activity.

## 3. Results and discussion

### 3.1. Textural features of the samples

Table 1 resumes the main textural properties of the prepared catalysts, obtained from both the powder XRD patterns and N<sub>2</sub> physisorption isotherms. Fig. 1A shows the wide-angle XRD spectra of the samples: the diffraction patterns are very similar and their indexing confirms the formation of a cubic fluorite lattice (*Fm3m* symmetry). These results are in agreement with litera-

ture, where the formation of a cubic (either cubic or tetragonal) solid solution for ceria–zirconia materials is generally favored for a greater Ce-content than 50 mol.% [37–39]. No peak splitting can be detected, thus confirming the formation of a single ceria–zirconia phase for all the samples. As expected, the XRD reflections of the Faujasite-type support (peaks denoted with “x”) also appear with the 50–Ce<sub>0.9</sub>Zr<sub>0.1</sub>O<sub>2</sub>–NP/FAU (the diffractograms of 25–Ce<sub>0.9</sub>Zr<sub>0.1</sub>O<sub>2</sub>–NP/FAU, and 75–Ce<sub>0.9</sub>Zr<sub>0.1</sub>O<sub>2</sub>–NP/FAU are not reported for the sake of brevity). The low-angle XRD pattern of the Ce<sub>0.9</sub>Zr<sub>0.1</sub>O<sub>2</sub>–M (Fig. 1B) shows that the replication of the KIT-6 template is well preserved, since the main (2 1 1) and (2 2 0) diffraction peaks of the silica template have appeared.

It is relatively difficult to evaluate the average particle size from Scherrer’s formula for nanoparticles that differ from a spherical geometry [40]. However, this estimation was performed to corroborate the TEM analysis. The application of Scherrer’s formula led to comparable sizes for the Ce<sub>x</sub>Zr<sub>1–x</sub>O<sub>2</sub>–NP samples, which consisted of crystallites with a diameter of about 16–18 nm (Table 1). On the other hand, slightly larger crystal sizes were obtained for the Ce<sub>0.9</sub>Zr<sub>0.1</sub>O<sub>2</sub>–SCS (~28 nm) and Ce<sub>0.9</sub>Zr<sub>0.1</sub>O<sub>2</sub>–M (~23 nm) samples.

The BET surface areas and the total pore volumes of the three Ce<sub>x</sub>Zr<sub>1–x</sub>O<sub>2</sub>–NP samples are very low (data shown in Table 1). On the other hand, the 25-, 50-, and 75–Ce<sub>0.9</sub>Zr<sub>0.1</sub>O<sub>2</sub>–NP/FAU exhibits better textural properties (S<sub>BET</sub> = 236–546 m<sup>2</sup> g<sup>–1</sup> and V<sub>p</sub> = 0.18–0.26 cm<sup>3</sup> g<sup>–1</sup>) than Ce<sub>0.9</sub>Zr<sub>0.1</sub>O<sub>2</sub>–NP, due to the high-surface-area of FAU-zeolite, which has a three-dimensional (3-D) network with cavities of molecular dimensions. The Faujasite framework consists of sodalite cages connected through hexagonal prisms. The pores are arranged perpendicular to each other. Each pore, which is formed by a 12-membered ring, has a relatively large diameter of 7.4 Å. The inner cavity has a diameter of 12 Å and is surrounded by 10 sodalite cages [41]. Thus, the FAU-type support may promote the oxidation activity of Ce–Zr mixed oxides, allow a better dispersion of the active phase on the external surface and store oxygen in the framework. Longer residence times of the gaseous molecules in the 3-D cavities should appear, thus, favoring total oxidation reactions [42]. Moreover, radical species may be formed during soot oxidation reaction and their collisions with the pore walls (and catalyst particles) influence the energy exchange [43].

The Ce<sub>0.9</sub>Zr<sub>0.1</sub>O<sub>2</sub>–M sample exhibits a BET surface area of 121 m<sup>2</sup> g<sup>–1</sup> and a total pore volume of 0.24 cm<sup>3</sup> g<sup>–1</sup>. These textural values are much lower than those of the employed KIT-6 silica template (S<sub>BET</sub> = 710 m<sup>2</sup> g<sup>–1</sup> and V<sub>p</sub> = 1.03 cm<sup>3</sup> g<sup>–1</sup>), as already observed in other studies on ceria-based materials obtained by nanocasting with mesoporous silica [44,45].

Fig. 2 shows N<sub>2</sub> isotherms at –196 °C of the Ce<sub>0.9</sub>Zr<sub>0.1</sub>O<sub>2</sub>–M and 50–Ce<sub>0.9</sub>Zr<sub>0.1</sub>O<sub>2</sub>/FAU samples: the former (curve a) displays type IV isotherms, which is typical of mesoporous materials (adsorption jump at *p/p*° ≈ 0.8–0.9), whereas, the latter (curve b) is characterized by type I isotherms, with a very steep uptake at low relative pressures (micropore filling), followed by a plateau to near satu-

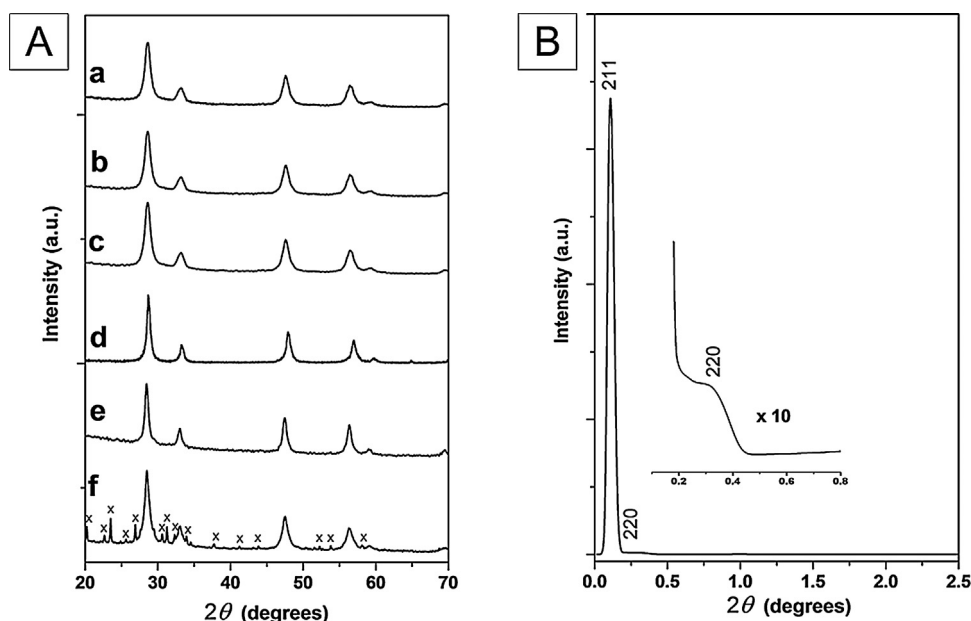


**Fig. 1.** Section (A): wide-angle XRD patterns of (a)  $\text{Ce}_{0.9}\text{Zr}_{0.1}\text{O}_2$ -NP, (b)  $\text{Ce}_{0.8}\text{Zr}_{0.2}\text{O}_2$ -NP, (c)  $\text{Ce}_{0.7}\text{Zr}_{0.3}\text{O}_2$ -NP, (d)  $\text{Ce}_{0.9}\text{Zr}_{0.1}\text{O}_2$ -M, (e)  $\text{Ce}_{0.9}\text{Zr}_{0.1}\text{O}_2$ -SCS, and (f) 50- $\text{Ce}_{0.9}\text{Zr}_{0.1}\text{O}_2$ -NP/FAU. Section (B): low-angle XRD of the  $\text{Ce}_{0.9}\text{Zr}_{0.1}\text{O}_2$ -M sample.

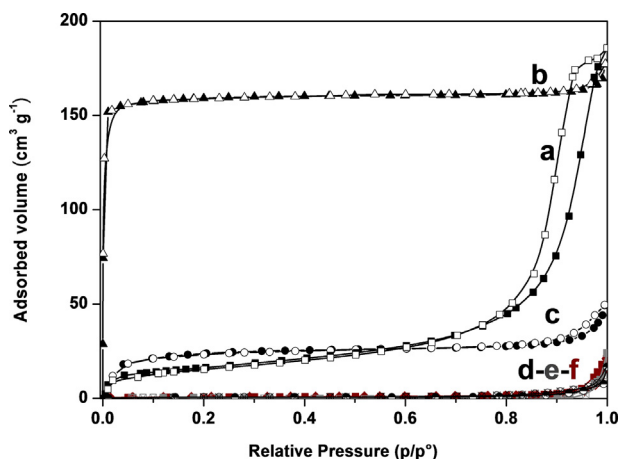
ration pressure. Worse textural properties were obtained for the  $\text{Ce}_{0.9}\text{Zr}_{0.1}\text{O}_2$ -SCS sample (data in Table 1), as confirmed by the shape of the adsorption isotherms (curve c). Finally, a much lower adsorption capacity can be observed for  $\text{Ce}_{0.9}\text{Zr}_{0.1}\text{O}_2$ -NP (curve d),  $\text{Ce}_{0.8}\text{Zr}_{0.2}\text{O}_2$ -NP (curve e), and  $\text{Ce}_{0.7}\text{Zr}_{0.3}\text{O}_2$ -NP (curve f), due to their very low surface areas and total pore volumes.

Electron microscopy analyses have been carried out to study the morphological features of the prepared samples. FESEM micrographs of the  $\text{Ce}_{0.9}\text{Zr}_{0.1}\text{O}_2$ -NP,  $\text{Ce}_{0.8}\text{Zr}_{0.2}\text{O}_2$ -NP, and  $\text{Ce}_{0.7}\text{Zr}_{0.3}\text{O}_2$ -NP samples (Fig. 3a–c, respectively) showed the presence of aggregates of particles in the range between 20 and 80 nm. A fairly good dispersion of  $\text{Ce}_{0.9}\text{Zr}_{0.1}\text{O}_2$ -NP on the FAU surface was observed for 50- $\text{Ce}_{0.9}\text{Zr}_{0.1}\text{O}_2$ -NP/FAU (Fig. 3d) (comparable FESEM images were obtained for both the 25- and 75- $\text{Ce}_{0.9}\text{Zr}_{0.1}\text{O}_2$ -NP/FAU samples). However, the lower BET surface area for the 75- $\text{Ce}_{0.9}\text{Zr}_{0.1}\text{O}_2$ -NP/FAU sample suggests the presence of multi-layers of the active phase over the FAU surface. This means that there will

be fewer soot-catalyst contact points and the molecular oxygen cannot easily reach the ceria–zirconia phase to be activated.

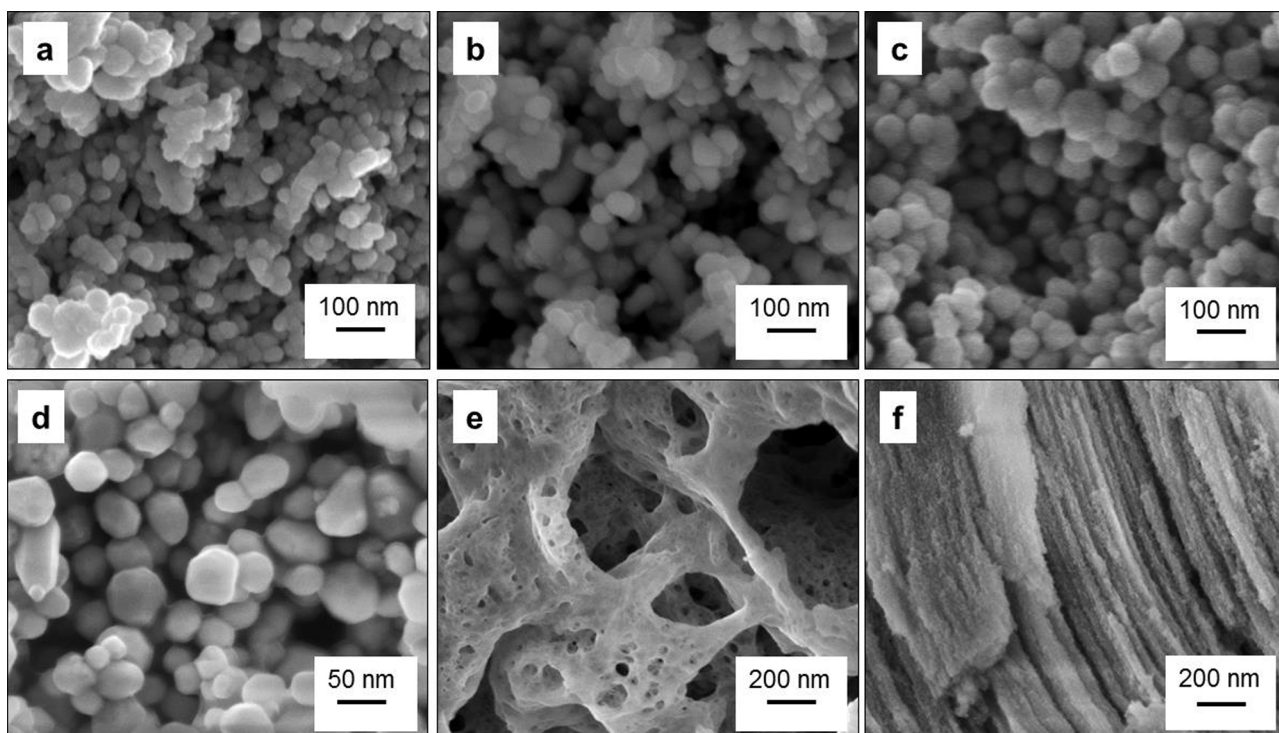
Larger inner cavities, due to the 3-D self-assembled nanoparticles, can be observed for the  $\text{Ce}_{0.9}\text{Zr}_{0.1}\text{O}_2$ -SCS sample (Fig. 3e). In the present case, the pore size is due to interparticle voids rather than to intraparticle porosity; in fact, the contribution of the pore volume is trivial ( $0.03 \text{ cm}^3 \text{ g}^{-1}$ ). Conversely, the  $\text{Ce}_{0.9}\text{Zr}_{0.1}\text{O}_2$ -M sample (Fig. 3f) shows the periodic ordered channels of the Ce–Zr mixed oxide, in agreement with the low-angle XRD results (*vide supra*). Energy dispersive X-ray analysis (EDS) indicated the complete removal of the silica template from the washed  $\text{Ce}_{0.9}\text{Zr}_{0.1}\text{O}_2$ -M (<1 wt.% Si).

Fig. 4a–c shows representative TEM images of the  $\text{Ce}_x\text{Zr}_{1-x}\text{O}_2$ -NP samples. A careful morphological analysis of these materials reveals the presence of nano-polyhedra (convex particles with the Euler characteristic of the sphere,  $X=2$ ) with sizes of ca. 20–40 nm. These particles are dominated by various crystallographic faces, which exhibit different surface atom densities, electronic structure, bonding, chemical reactivities and thermodynamic properties. The micrograph in Fig. 4a shows a  $\text{Ce}_{0.9}\text{Zr}_{0.1}\text{O}_2$ -NP oriented along the (100) direction with (100)-type planes at  $90^\circ$ , as reflected by the Fourier Transform image. The (110) planes that originate from the truncation of the particle edges can also be seen at  $45^\circ$ . Similar shapes can be observed for both  $\text{Ce}_{0.8}\text{Zr}_{0.2}\text{O}_2$ -NP and  $\text{Ce}_{0.7}\text{Zr}_{0.3}\text{O}_2$ -NP (Fig. 4b and c, respectively). These convex structures are the result of the optimized surface energy, and they may form several polyhedra (e.g., truncated cube, cuboctahedron, etc.), as observed for pure ceria nanocatalysts [1,31,46]. The equilibrium shape of these nanoparticles is determined by the Wulff rule [47], according to which the convex envelope of planes (perpendicular to the surface normal) minimizes the surface energy for a given enclosed volume. In particular, the presence of planes with higher Miller indices in truncated polyhedra, such as the (110) surfaces, seems to have a beneficial effect on surface reactivity [10]. On the other hand, non-convex particles ( $X \neq 2$ ), like Kepler–Poinsot polyhedral, should also appear as a consequence of selective passivation and the blocking of edge and corner sites during growth, coupled with anisotropic growth rates in different orientations.



**Fig. 2.**  $\text{N}_2$  physisorption isotherms measured at  $-196^\circ\text{C}$  on samples previously outgassed at  $200^\circ\text{C}$ : (a)  $\text{Ce}_{0.9}\text{Zr}_{0.1}\text{O}_2$ -M, (b) 50- $\text{Ce}_{0.9}\text{Zr}_{0.1}\text{O}_2$ -NP/FAU, (c)  $\text{Ce}_{0.9}\text{Zr}_{0.1}\text{O}_2$ -SCS, (d)  $\text{Ce}_{0.9}\text{Zr}_{0.1}\text{O}_2$ -NP, (e)  $\text{Ce}_{0.8}\text{Zr}_{0.2}\text{O}_2$ -NP, and (f)  $\text{Ce}_{0.7}\text{Zr}_{0.3}\text{O}_2$ -NP. Full symbols: adsorption branch; white symbols: desorption branch.





**Fig. 3.** FESEM images of (a)  $\text{Ce}_{0.9}\text{Zr}_{0.1}\text{O}_2\text{-NP}$ , (b)  $\text{Ce}_{0.8}\text{Zr}_{0.2}\text{O}_2\text{-NP}$ , (c)  $\text{Ce}_{0.7}\text{Zr}_{0.3}\text{O}_2\text{-NP}$ , (d)  $50\text{-Ce}_{0.9}\text{Zr}_{0.1}\text{O}_2\text{-NP/FAU}$ , (e)  $\text{Ce}_{0.9}\text{Zr}_{0.1}\text{O}_2\text{-SCS}$ , and (f)  $\text{Ce}_{0.9}\text{Zr}_{0.1}\text{O}_2\text{-M}$ .

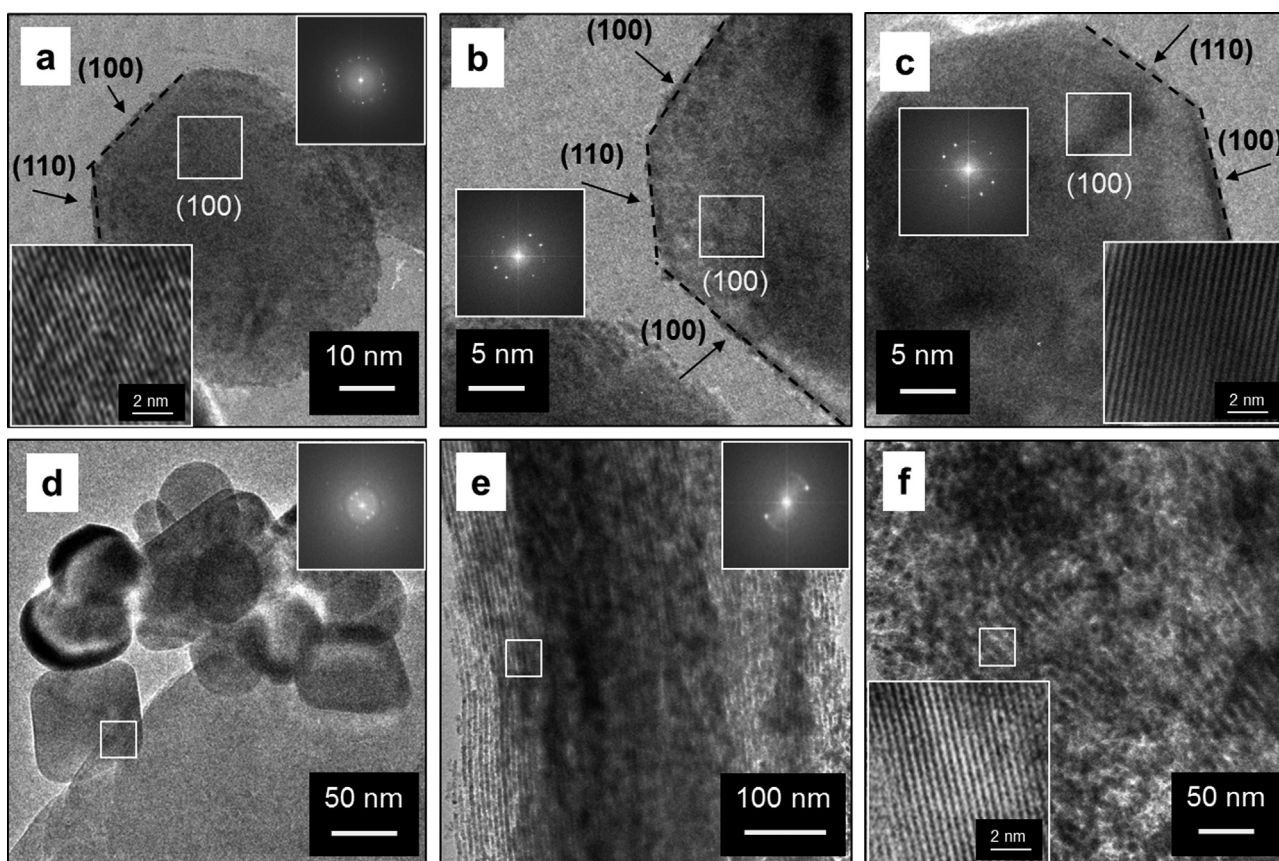


**Fig. 4.** TEM images of the (a)  $\text{Ce}_{0.9}\text{Zr}_{0.1}\text{O}_2\text{-NP}$ , (b)  $\text{Ce}_{0.8}\text{Zr}_{0.2}\text{O}_2\text{-NP}$ , (c)  $\text{Ce}_{0.7}\text{Zr}_{0.3}\text{O}_2\text{-NP}$ , (d)  $50\text{-Ce}_{0.9}\text{Zr}_{0.1}\text{O}_2\text{-NP/FAU}$  and (e and f)  $\text{Ce}_{0.9}\text{Zr}_{0.1}\text{O}_2\text{-M}$  samples.

A TEM image of the 50-Ce<sub>0.9</sub>Zr<sub>0.1</sub>O<sub>2</sub>-NP/FAU sample is shown in Fig. 4d. The latter micrograph confirms a good dispersion of Ce<sub>0.9</sub>Zr<sub>0.1</sub>O<sub>2</sub>-NP over the FAU surface. Moreover, the overlapping of particles (=aggregate) gives rise to 3-D self-assembled arrays that are spatially accessible to reactants. The interactions between the soot particles and the catalyst increase, thus favoring the overall catalytic activity.

TEM images of the Ce<sub>0.9</sub>Zr<sub>0.1</sub>O<sub>2</sub>-M sample are shown in Fig. 4e and f. This sample exhibits ordered mesopores, and the evenly spaced parallel channels confirm a well-developed long-range order, in agreement with the XRD analysis. These nanoparticles are highly crystalline and display an interplanar spacing of ca. 0.30 nm, corresponding to the (1 1 1) lattice planes. The pore wall thickness estimated from the TEM images was about 8 nm, which is slightly more than the 6 nm calculated with the BET method. The TEM images of Ce<sub>0.9</sub>Zr<sub>0.1</sub>O<sub>2</sub>-SCS (not reported for the sake of brevity) shows the presence of 15–20 nm particles.

### 3.2. Reducibility and redox properties of ceria–zirconia materials

The reduction behavior of ceria–zirconia materials has been studied by means of H<sub>2</sub>-TPR analysis. According to the literature, hydrogen temperature-programmed reduction measurements give valuable indications on the reducibility and the redox behavior of CeO<sub>2</sub>-based materials [1,16,48].

The reduction in CeO<sub>2</sub> occurs via a stepwise mechanism, in which there is a first reduction of the outer layer of the Ce species (surface reduction) and then a reduction of the inner layers (bulk reduction) at higher temperatures [49].

However, with low-surface-area ceria, the reduction at low temperatures is often negligible, and a main peak, due to bulk CeO<sub>2</sub> reduction, usually occurs above 700 °C [31]. The incorporation of non-reducible Zr<sup>4+</sup> ions into the CeO<sub>2</sub> lattice has been shown to affect the redox properties, and hence the capacity of a material to release oxygen under reducing conditions. This means that H<sub>2</sub>-TPR profiles of ceria–zirconia materials are much more complex than those of pure ceria, since different factors (e.g., the Zr/Ce ratio, structural defects, changes in electronic structure, and so on) all contribute. Zr-doped ceria does not usually show surface or bulk reduction peaks, but rather a broad signal in a wide-temperature range; this TPR profile is a consequence of the high mobility of lattice oxygen within the solid, since once the surface Ce<sup>4+</sup> cations are reduced, bulk oxygen migrates rapidly to the surface and the reduction process continues [4].

Fig. 5 shows the H<sub>2</sub>-TPR profiles of the fresh catalysts. The main reduction peaks for Ce<sub>0.9</sub>Zr<sub>0.1</sub>O<sub>2</sub>-NP (curve a), Ce<sub>0.8</sub>Zr<sub>0.2</sub>O<sub>2</sub>-NP (curve b) and Ce<sub>0.7</sub>Zr<sub>0.3</sub>O<sub>2</sub>-NP (curve c) are centered at 549, 565, and 577 °C, respectively. The temperature of these signals increases as the Zr-content increases, thus, confirming the beneficial role of Zr<sup>4+</sup> cations on the reduction resistance of ceria. A similar TPR profile has been obtained with the Ce<sub>0.9</sub>Zr<sub>0.1</sub>O<sub>2</sub>-NP/FAU sample (curve d), where the reduction peak occurs at 558 °C. On the other hand, higher reduction temperatures can be observed for both Ce<sub>0.9</sub>Zr<sub>0.1</sub>O<sub>2</sub>-M (curve e) and Ce<sub>0.9</sub>Zr<sub>0.1</sub>O<sub>2</sub>-SCS (curve f), namely at 603 and 588 °C, respectively. These results suggest a higher mobility of lattice oxygen within the Ce<sub>x</sub>Zr<sub>1-x</sub>O<sub>2</sub>-NP catalysts (especially in Ce<sub>0.9</sub>Zr<sub>0.1</sub>O<sub>2</sub>-NP), and hence easier reducibility compared to high-surface area ceria–zirconia systems.

Fig. 6 report the XPS spectra in the O 1s, Ce, and Zr 3d BE regions. The O 1s spectra (Fig. 6A) shows different peaks, which have been assigned to either chemisorbed oxygen (O<sub>α</sub> species) or lattice oxygen (O<sub>β</sub> species). The peak at 528.6–528.9 eV corresponds to O<sub>β</sub> (i.e., O<sup>2-</sup>), whereas, the signal at 529.9–531.4 eV can be ascribed to surface oxygens (i.e., O<sub>2</sub><sup>2-</sup>, O<sup>-</sup>, OH<sup>-</sup>, CO<sub>3</sub><sup>2-</sup>) [44,50]. The presence of Na impurities (although in the 0.1–0.3 wt.% range) could

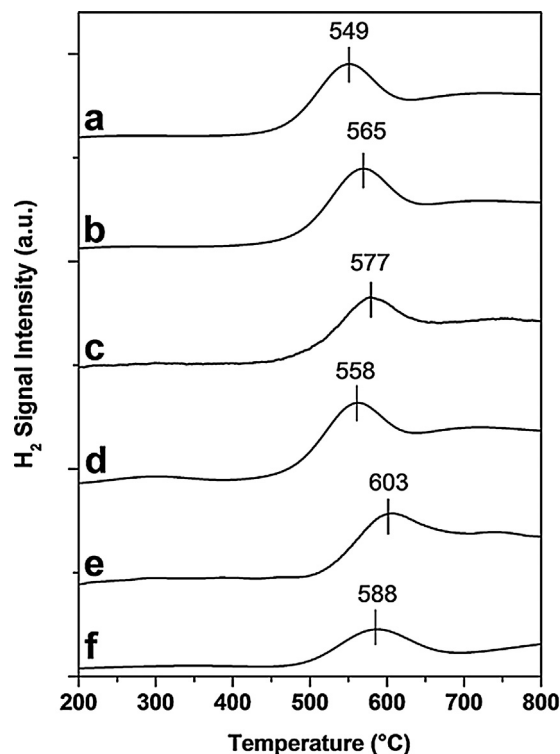


Fig. 5. H<sub>2</sub>-TPR profiles of the (a) Ce<sub>0.9</sub>Zr<sub>0.1</sub>O<sub>2</sub>-NP, (b) Ce<sub>0.8</sub>Zr<sub>0.2</sub>O<sub>2</sub>-NP, (c) Ce<sub>0.7</sub>Zr<sub>0.3</sub>O<sub>2</sub>-NP, (d) 50-Ce<sub>0.9</sub>Zr<sub>0.1</sub>O<sub>2</sub>-NP/FAU, (e) Ce<sub>0.9</sub>Zr<sub>0.1</sub>O<sub>2</sub>-M, and (f) Ce<sub>0.9</sub>Zr<sub>0.1</sub>O<sub>2</sub>-SCS samples.

explain the different BE shifts, since the low electronegativity of alkaline metals leads to a high negative charge density transfer to oxide anions. With the Ce<sub>0.9</sub>Zr<sub>0.1</sub>O<sub>2</sub>-NP sample, the peak due to the O<sub>β</sub> species appears at a slightly higher BE (528.9 eV), thus, suggesting a lower nucleophilicity of the lattice oxygen ions. On the other hand, electrophilic oxygen species (O<sub>α</sub>) are usually involved in total oxidation reactions, and may give rise to beneficial spillover phenomena on the catalytic surface [51].

As a whole, spillover oxygen can play different roles in oxidation catalysis, in that it may: (i) control the active centers (namely formation and regeneration) and (ii) serve as a reactant. This means that when catalytic sites are irrigated by spillover oxygen (the so-called “active oxygen”), the catalytic surface becomes very efficient in the soot combustion reaction.

As shown in Table 2, higher O<sub>α</sub>/O<sub>β</sub> ratios have been obtained for high-surface area materials than for Ce<sub>x</sub>Zr<sub>1-x</sub>O<sub>2</sub>-NP, due to the higher amounts of surface hydroxyls, carbonates, and adsorbed molecular oxygen.

Conversely, Ce<sub>x</sub>Zr<sub>1-x</sub>O<sub>2</sub>-NP mainly exhibit O<sub>β</sub> species, which play a role in the oxidation reactions that are kinetically described through a Mars-van Krevelen (MvK) mechanism; these reactions take place in the 300–500 °C range, according to Golodets’ classification [52]. Similarly, Bueno-López et al. [53] have demonstrated that lattice oxygen is the “active oxygen” for soot oxidation at moderate temperatures (350–500 °C).

At low temperatures, only the outer catalyst layer may be equilibrated with oxygen in the gas-phase; at high temperatures, surface defects diffuse in the bulk, and equilibrium is reached between the gas-phase and the solid oxide. The dissociative adsorption of molecular oxygen, in fact requires successive electron transfers from the solid catalyst into the anti-bonding  $\pi$ -orbital of the molecule until cleavage of the O–O bond is reached:

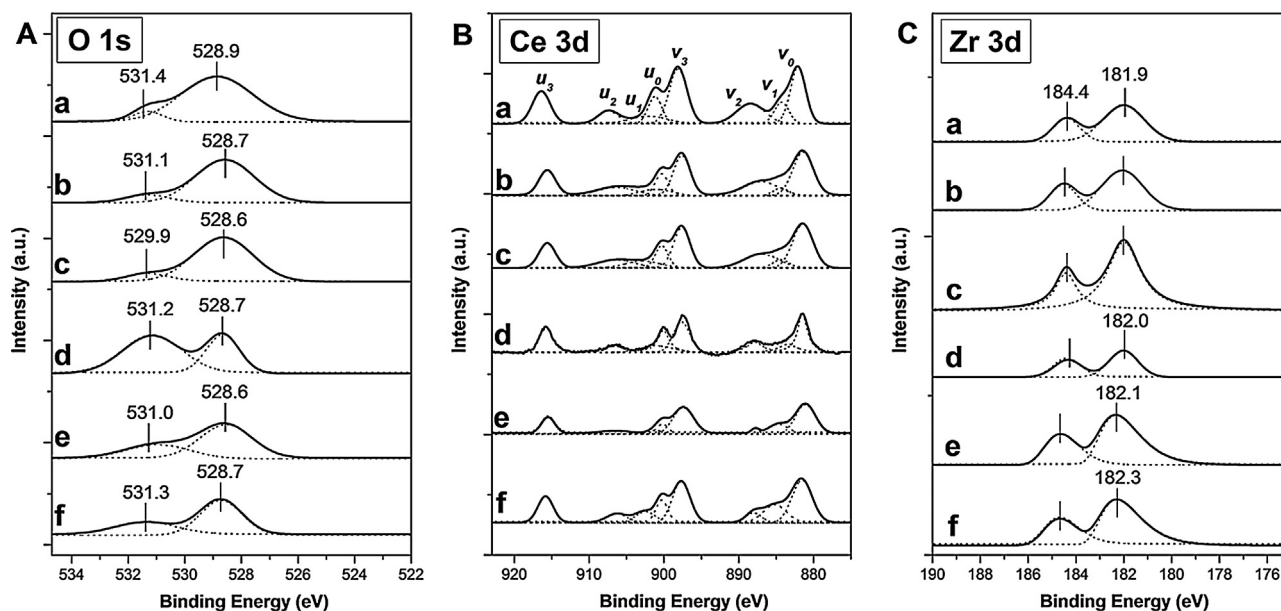
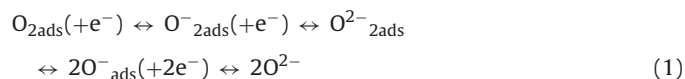


**Fig. 6.** XPS spectra of the (a)  $\text{Ce}_{0.9}\text{Zr}_{0.1}\text{O}_2\text{-NP}$ , (b)  $\text{Ce}_{0.8}\text{Zr}_{0.2}\text{O}_2\text{-NP}$ , (c)  $\text{Ce}_{0.7}\text{Zr}_{0.3}\text{O}_2\text{-NP}$ , (d)  $50\text{-Ce}_{0.9}\text{Zr}_{0.1}\text{O}_2\text{-NP/FAU}$ , (e)  $\text{Ce}_{0.9}\text{Zr}_{0.1}\text{O}_2\text{-M}$  and (f)  $\text{Ce}_{0.9}\text{Zr}_{0.1}\text{O}_2\text{-SCS}$  samples in the O 1s (Section A), Ce 3d (Section B), and Zr 3d (Section C) core level regions (Section C).

**Table 2**

Results of curve-fittings on the O 1s binding energy of catalysts. The relative ratios of the surface-adsorbed oxygen ( $\text{O}_\alpha$ ) and lattice oxygen ( $\text{O}_\beta$ ) are reported in the last column.

Sample	$\text{O}_\alpha$ (% atom)	$\text{O}_\alpha$ BE (eV)	$\text{O}_\beta$ (% atom)	$\text{O}_\beta$ BE (eV)	$\text{O}_\alpha/\text{O}_\beta$
$\text{Ce}_{0.9}\text{Zr}_{0.1}\text{O}_2\text{-NP}$	8.9	531.4	91.1	528.9	0.10
$\text{Ce}_{0.8}\text{Zr}_{0.2}\text{O}_2\text{-NP}$	11.0	531.1	89.0	528.7	0.12
$\text{Ce}_{0.7}\text{Zr}_{0.3}\text{O}_2\text{-NP}$	11.3	531.0	88.7	528.6	0.13
$50\text{-Ce}_{0.9}\text{Zr}_{0.1}\text{O}_2\text{-NP/FAU}$	36.3	531.2	63.7	528.7	0.57
$\text{Ce}_{0.9}\text{Zr}_{0.1}\text{O}_2\text{-M}$	34.3	531.0	65.7	528.6	0.52
$\text{Ce}_{0.9}\text{Zr}_{0.1}\text{O}_2\text{-SCS}$	33.5	531.3	66.5	528.7	0.50



The diffusivity of oxide ions is an important condition in the oxygen storage/release process of ceria-based catalysts. According to literature [1], the diffusion coefficient of O atoms in Ce–Zr mixed oxides is higher than in pure ceria. This electronic property is very important in oxidation catalysis, since the requirements for the MvK mechanism to take place comprise a good mobility of both

electrons and lattice oxygen anions within the solid catalyst. The MvK mechanism in fact involves two redox processes, one consisting of the injection of electrons into the catalyst, the other involving the extraction of electrons from the oxide. These processes can take place spontaneously if two conditions are met: (i) the highest occupied molecular orbital of the hydrocarbon is above the bottom of the unoccupied conduction band (CB), thus allowing the transfer of electrons from adsorbed soot/hydrocarbons to the catalyst; (ii) the unoccupied molecular orbitals of  $\text{O}_2$  must be level with the

**Table 3A**

Results of curve-fittings on the Ce 3d binding energy of catalysts.

Ce 3d <sub>5/2</sub>								
Sample	$\nu_0$ ( $\text{Ce}^{4+}$ ) (% at.)	$\nu_0$ ( $\text{Ce}^{4+}$ ) BE (eV)	$\nu_1$ ( $\text{Ce}^{3+}$ ) (% at.)	$\nu_1$ ( $\text{Ce}^{3+}$ ) BE (eV)	$\nu_2$ ( $\text{Ce}^{4+}$ ) (% at.)	$\nu_2$ ( $\text{Ce}^{4+}$ ) BE (eV)	$\nu_3$ ( $\text{Ce}^{4+}$ ) (% at.)	$\nu_3$ ( $\text{Ce}^{4+}$ ) BE (eV)
$\text{Ce}_{0.9}\text{Zr}_{0.1}\text{O}_2\text{-NP}$	20.3	882.1	7.4	884.3	13.4	888.4	23.6	898.1
$\text{Ce}_{0.8}\text{Zr}_{0.2}\text{O}_2\text{-NP}$	24.7	881.8	4.1	884.6	10.0	888.3	20.3	897.9
$\text{Ce}_{0.7}\text{Zr}_{0.3}\text{O}_2\text{-NP}$	26.5	881.4	3.8	884.3	14.4	886.9	19.7	897.6
$50\text{-Ce}_{0.9}\text{Zr}_{0.1}\text{O}_2\text{-NP/FAU}$	26.6	881.4	2.9	884.2	10.5	886.8	24.3	897.6
$\text{Ce}_{0.9}\text{Zr}_{0.1}\text{O}_2\text{-M}$	32.6	881.1	9.9	884.7	2.1	887.8	29.9	897.4
$\text{Ce}_{0.9}\text{Zr}_{0.1}\text{O}_2\text{-SCS}$	27.1	881.6	12.5	885.2	4.5	888.1	22.9	897.7
Ce 3d <sub>3/2</sub>								
Sample	$u_0$ ( $\text{Ce}^{4+}$ ) (% at.)	$u_0$ ( $\text{Ce}^{4+}$ ) BE (eV)	$u_1$ ( $\text{Ce}^{3+}$ ) (% at.)	$u_1$ ( $\text{Ce}^{3+}$ ) BE (eV)	$u_2$ ( $\text{Ce}^{4+}$ ) (% at.)	$u_2$ ( $\text{Ce}^{4+}$ ) BE (eV)	$u_3$ ( $\text{Ce}^{4+}$ ) (% at.)	$u_3$ ( $\text{Ce}^{4+}$ ) BE (eV)
$\text{Ce}_{0.9}\text{Zr}_{0.1}\text{O}_2\text{-NP}$	8.8	901.2	6.5	902.1	6.1	907.4	13.9	916.4
$\text{Ce}_{0.8}\text{Zr}_{0.2}\text{O}_2\text{-NP}$	7.3	900.4	7.0	901.9	12.1	906.7	14.4	915.8
$\text{Ce}_{0.7}\text{Zr}_{0.3}\text{O}_2\text{-NP}$	6.9	900.3	6.7	901.1	9.3	906.3	12.7	915.6
$50\text{-Ce}_{0.9}\text{Zr}_{0.1}\text{O}_2\text{-NP/FAU}$	8.1	900.2	5.4	901.1	8.7	906.3	13.5	915.5
$\text{Ce}_{0.9}\text{Zr}_{0.1}\text{O}_2\text{-M}$	6.2	900.2	2.8	901.2	4.3	906.6	12.8	915.5
$\text{Ce}_{0.9}\text{Zr}_{0.1}\text{O}_2\text{-SCS}$	7.6	900.3	7.2	902.5	5.4	906.3	12.8	915.8

**Table 3B**

Results of curve-fittings on the Ce 3d binding energy of catalysts.

Sample	Ce <sup>3+</sup> ( $\nu_1 + u_1$ ) (% at.)
Ce <sub>0.9</sub> Zr <sub>0.1</sub> O <sub>2</sub> -NP	13.9
Ce <sub>0.8</sub> Zr <sub>0.2</sub> O <sub>2</sub> -NP	11.1
Ce <sub>0.7</sub> Zr <sub>0.3</sub> O <sub>2</sub> -NP	10.5
50-Ce <sub>0.9</sub> Zr <sub>0.1</sub> O <sub>2</sub> -NP/FAU	8.3
Ce <sub>0.9</sub> Zr <sub>0.1</sub> O <sub>2</sub> -M	12.6
Ce <sub>0.9</sub> Zr <sub>0.1</sub> O <sub>2</sub> -SCS	19.7

occupied states in the valence band, to ensure transfer from the solid.

Fig. 6B shows the Ce 3d core-level spectra of the samples, where the “ $\nu$ ” and “ $u$ ” peaks correspond to the 3d<sub>5/2</sub> and 3d<sub>3/2</sub> states, respectively. The doublets ( $\nu_0, u_0$ ), ( $\nu_2, u_2$ ), and ( $\nu_3, u_3$ ) are assigned to the diversified states of Ce<sup>4+</sup>, whereas the doublet ( $\nu_1, u_1$ ) is due to the Ce<sup>3+</sup> species [50]. Table 3A reports the relative abundance of the Ce<sup>3+</sup> and Ce<sup>4+</sup> species for each sample maintained under partial reducing conditions (ultra-high vacuum and electron beam irradiation), which is estimated considering the deconvolution results of Ce 3d. As summarized in Table 3B, the relative amount of Ce<sup>3+</sup> (at.%) decreases for an increase in the Zr content (namely, the Ce<sup>3+</sup> content = 13.9, 11.2, and 10.6% for Ce<sub>0.9</sub>Zr<sub>0.1</sub>O<sub>2</sub>-NP, Ce<sub>0.8</sub>Zr<sub>0.2</sub>O<sub>2</sub>-NP, and Ce<sub>0.7</sub>Zr<sub>0.3</sub>O<sub>2</sub>-NP, respectively), thus, suggesting the role of Zr<sup>4+</sup> ions in maintaining a higher oxidation state of the Ce species [54]. The Ce<sup>3+</sup> content of Ce<sub>0.9</sub>Zr<sub>0.1</sub>O<sub>2</sub>-SCS (19.7%) is higher than that of the other samples, due to the higher temperature used during the combustion synthesis (600 °C) [51]. Finally, Fig. 6C shows the Zr 3d spectra: the peaks at 181.9–182.3 eV denote the Zr 3d<sub>5/2</sub> states, whereas, the signals at 184.4 eV correspond to the Zr 3d<sub>3/2</sub> levels. According to the BE of Zr 3d<sub>5/2</sub>, Ce–Zr mixed oxide can be well-distinguished from the ZrO<sub>2</sub> phase (182.9 eV [55,56]). As a whole, no signal due to the ZrO<sub>2</sub> phase has been detected for any of the ceria–zirconia samples. The intensity of the Zr 3d peak increased as the Zr-content increased for Ce<sub>x</sub>Zr<sub>1-x</sub>O<sub>2</sub>-NP, but no significant shift to a higher BE was observed. Therefore, it can be stated that a good incorporation of the Zr species into the ceria framework has been obtained for all the ceria–zirconia catalysts.

The Raman spectra of the ceria–zirconia catalysts are shown in Fig. 7A. The spectra of all samples are comparable and are characterized by the signals attributed to the symmetric breathing mode (F<sub>2g</sub>) of oxygen atoms around Ce<sup>4+</sup> ions at ca. 460 cm<sup>-1</sup> (characteristic of the fluorite structure) and a low-intensity band at ca. 600 cm<sup>-1</sup> due the presence of oxygen vacancies (O<sub>v</sub>) [57,58]. The ratio between the areas of the O<sub>v</sub> and F<sub>2g</sub> Raman bands is the most appropriate way to compare the population of oxygen vacancies in different solids: the higher the O<sub>v</sub>/F<sub>2g</sub> area ratio value the higher the number of oxygen vacancies [57–59].

The O<sub>v</sub>/F<sub>2g</sub> area ratio values obtained for the prepared ceria–zirconia catalysts (Fig. 7B) show that nano-polyhedra (Ce<sub>0.9</sub>Zr<sub>0.1</sub>O<sub>2</sub>-NP) have slightly higher oxygen vacancies than porous catalysts with the same Zr-content. The addition of Zr<sup>4+</sup> ions favors the formation of additional oxygen vacancies in the nano-polyhedra, especially with Zr 30 mol.%. On the other hand, the F<sub>2g</sub> band of CeO<sub>2</sub> is blue-shifted by 11 cm<sup>-1</sup> in the case of Ce<sub>0.7</sub>Zr<sub>0.3</sub>-NP, possibly due to the higher amount of Ce<sup>4+</sup> species as revealed by XPS measurements.

### 3.3. Soot oxidation activity

Over the years, several studies on ceria–zirconia catalysts have reported that, in the intermediate Ce–Zr composition range, there is an optimum balance between the amount of redox centers and the number of structural defects. Oxygen storage capacities typically exhibit a volcano-curve profile, as a function of the Ce/Zr ratio in ceria–zirconia solid solutions. On the basis of dynamic OSC measurements carried out in different laboratories, it has been observed that the position of the maximum OSC for Ce<sub>x</sub>Zr<sub>1-x</sub>O<sub>2</sub> materials shifts from  $x=0.5$  to 0.9 (the best OSC values are usually observed with ca. 80 mol.% of CeO<sub>2</sub>) [16]. However, the overall catalytic activity depends on several factors, such as the operating conditions, the soot-catalyst contact points and the structural parameters of the catalyst.

Thus, the catalytic activity of the prepared ceria–zirconia materials towards soot oxidation has been examined in the 100–700 °C temperature range, under both “loose” and “tight” contact con-

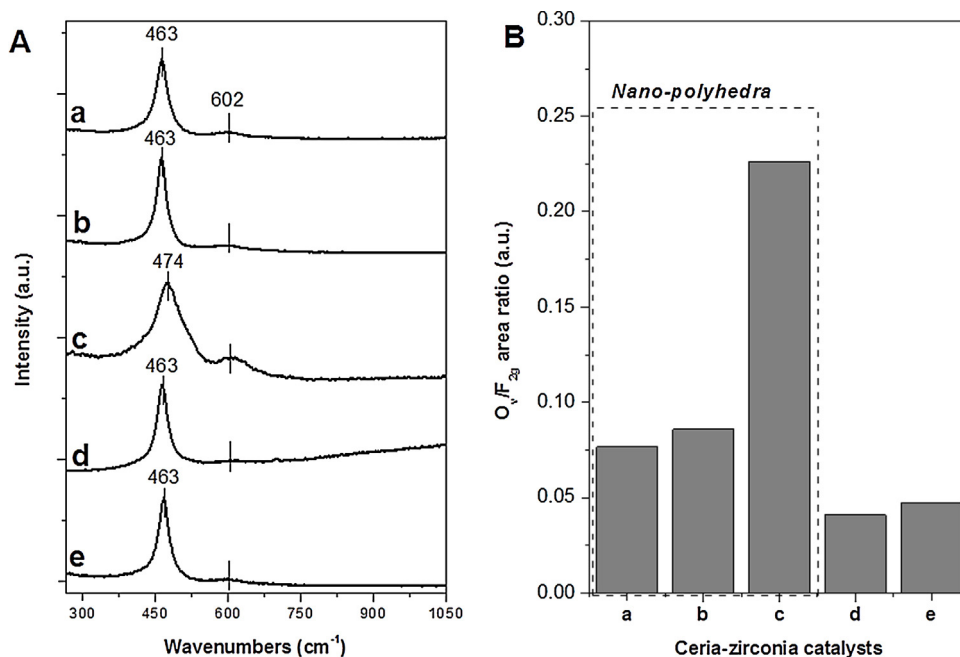


**Fig. 7.** Section (A) Raman spectra of the (a) Ce<sub>0.9</sub>Zr<sub>0.1</sub>O<sub>2</sub>-NP, (b) Ce<sub>0.8</sub>Zr<sub>0.2</sub>O<sub>2</sub>-NP, (c) Ce<sub>0.7</sub>Zr<sub>0.3</sub>O<sub>2</sub>-NP, (d) Ce<sub>0.9</sub>Zr<sub>0.1</sub>O<sub>2</sub>-M and (e) Ce<sub>0.9</sub>Zr<sub>0.1</sub>O<sub>2</sub>-SCS samples. Section (B) O<sub>v</sub>/F<sub>2g</sub> area ratios of the same catalysts.



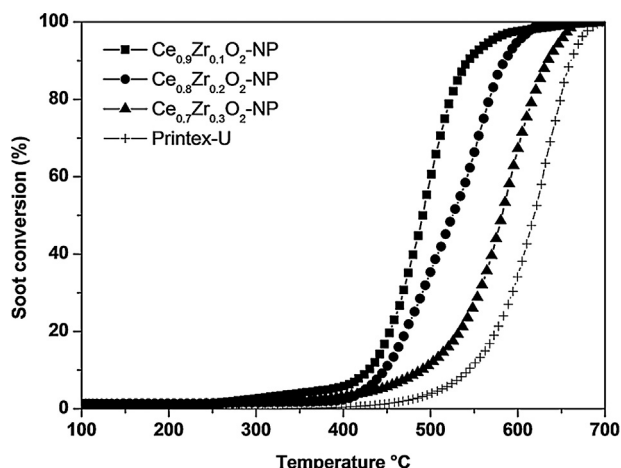


Fig. 8. Soot conversion (%), as a function of temperature, over the  $\text{Ce}_x\text{Zr}_{1-x}\text{O}_2$ -NP catalysts, and Printex-U (no catalyst) using “loose” soot-catalyst conditions.

ditions. Fig. 8 shows the soot conversion to  $\text{CO}_x$  as a function of the temperature achieved for the  $\text{Ce}_x\text{Zr}_{1-x}\text{O}_2$ -NP catalysts (in “loose” contact) along with Printex-U (no catalyst). As a whole, the three nanocatalysts exhibited positive soot conversion trends for an increasing reaction temperature, and soot combustion was completed at about 550 °C. Higher activities (in terms of  $T_{10\%}$ ,  $T_{50\%}$ , and  $T_{90\%}$  values) were reached for the  $\text{Ce}_{0.9}\text{Zr}_{0.1}\text{O}_2$ -NP catalyst, compared to  $\text{Ce}_{0.8}\text{Zr}_{0.2}\text{O}_2$ -NP and  $\text{Ce}_{0.7}\text{Zr}_{0.3}\text{O}_2$ -NP (values reported in Table 4). Therefore,  $\text{Ce}_{0.9}\text{Zr}_{0.1}\text{O}_2$ -NP appears to be the most active catalyst, likely due to its better redox properties and easier surface reducibility (*vide supra*). As is known, the higher specific activity towards soot combustion can be attributed to the easiness of the formation of oxygen vacancies on the more reactive surfaces [31]. The oxygen vacancies and  $\text{Ce}^{3+}$  species formed during the course of the catalytic reaction, once oxygen anions are transferred from catalysts to soot, play a key role in the promoter/catalyst properties of ceria.

The substitution of some  $\text{Ce}^{4+}$  (ionic radius of 0.97 Å) for  $\text{Zr}^{4+}$  ions (0.84 Å) favors the formation of defects (e.g., oxygen vacancies) in the ceria-zirconia lattice, thus inducing a distortion of the oxygen sublattice. However, the amount of active redox sites ( $\text{Ce}^{3+}/\text{Ce}^{4+}$ ) decreases as the Zr-content increases [16]. Moreover, the mobility of both electrons and lattice oxygen anions within the solid catalyst is favored for higher Ce contents (*vide supra*). It therefore seems that the incorporation of Zr into the ceria lattice does not have a direct beneficial effect on soot oxidation for catalysts calcined at low/mild temperature (namely, below 600 °C), since it decreases the population of surface redox-active centers, which are directly dependent on the surface density of the  $\text{Ce}^{3+}$ - $\text{Ce}^{4+}$  sites [13]. As a result, the best compromise between surface defects and redox features can be observed for the  $\text{Ce}_{0.9}\text{Zr}_{0.1}\text{O}_2$ -NP catalyst. Similarly, the differ-

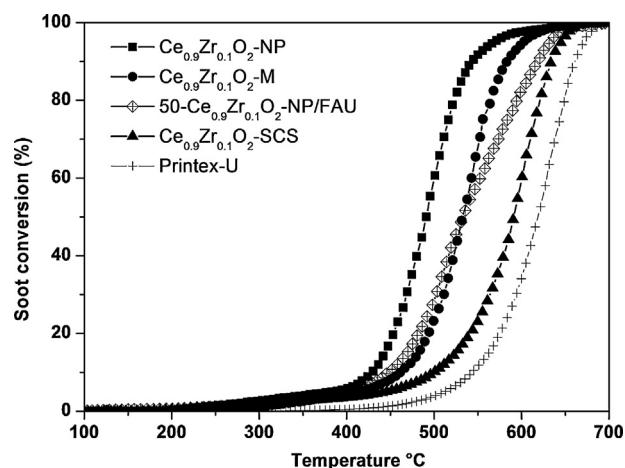


Fig. 9. Soot conversion (%), as a function of temperature, over the ceria-zirconia catalysts and Printex-U (no catalyst) using “loose” soot-catalyst conditions.

ent morphologies of the prepared catalysts (with an atomic ratio Ce/Zr = 0.9) have been tested to study the effect of topological and textural properties on the soot oxidation activity. Fig. 9 shows soot combustion as a function of the temperature obtained with the ceria-zirconia catalysts (in “loose” contact). The catalysts exhibited positive soot conversion trends for an increasing reaction temperature, and soot combustion was completed at about 620 °C for the least active catalyst (namely  $\text{Ce}_{0.9}\text{Zr}_{0.1}\text{O}_2$ -SCS). Once again, the best performances was achieved with  $\text{Ce}_{0.9}\text{Zr}_{0.1}\text{O}_2$ -NP, although the latter catalyst provided the lowest specific surface area. This result is in fair agreement with the literature, according to which ceria-based materials, with exposed highly reactive planes, may lead to high conversions despite their low surface areas [31,60]. Indeed, the  $\text{Ce}_{0.9}\text{Zr}_{0.1}\text{O}_2$ -NP catalyst exhibits nano-polyhedra with several (110) and (100) reactive planes, as revealed by XRD and TEM analyses. Similarly, higher amounts of  $\text{O}_v$  have been observed for the  $\text{Ce}_x\text{Zr}_{1-x}\text{O}_2$ -NP catalysts, with respect to  $\text{Ce}_{0.9}\text{Zr}_{0.1}\text{O}_2$ -M and  $\text{Ce}_{0.9}\text{Zr}_{0.1}\text{O}_2$ -SCS (*vide supra*).

The relative number of low coordination surface sites (e.g., edge and corner atoms) increases with decreasing particle size, and hence the surface reactivity grows in the nanoscale domain. Larger-sized particles usually show a lower density of the crystalline defects [20]. On the other hand, various catalytic results have been reported over the years for ceria-based materials [60–63], likely due to the fact that (i) the BET surface area can be different from the “accessible surface area” (the actual outside surface area) [53,60–64] and (ii) it is not possible, in complex gas–solid systems, to select a single property to explain the overall activity [4].

Comparable results have been obtained for the  $\text{Ce}_{0.9}\text{Zr}_{0.1}\text{O}_2$ -M and 50- $\text{Ce}_{0.9}\text{Zr}_{0.1}\text{O}_2$ -NP/FAU catalysts. However, the higher surface area (=more surface oxygens) of the latter catalyst seems to play a beneficial role at low temperatures (e.g., in terms of onset temperature), whereas, better performances in terms of  $T_{50\%}$  and  $T_{90\%}$  can be reached with  $\text{Ce}_{0.9}\text{Zr}_{0.1}\text{O}_2$ -M, due to the higher amount of the active phase. Conversely, the  $\text{Ce}_{0.9}\text{Zr}_{0.1}\text{O}_2$ -SCS catalyst exhibited worse soot conversion values than the other porous samples (50- $\text{Ce}_{0.9}\text{Zr}_{0.1}\text{O}_2$ -FAU and  $\text{Ce}_{0.9}\text{Zr}_{0.1}\text{O}_2$ -M), thus, confirming the important role of micro-/mesoporosity for this oxidation process. As shown in Fig. 10, the higher amount of the  $\text{Ce}_{0.9}\text{Zr}_{0.1}\text{O}_2$ -NP on the FAU-type support (namely 75- $\text{Ce}_{0.9}\text{Zr}_{0.1}\text{O}_2$ -NP/FAU) does not significantly improve the catalytic activity (in terms of  $T_{50\%}$  and  $T_{90\%}$ ) compared to that of 50- $\text{Ce}_{0.9}\text{Zr}_{0.1}\text{O}_2$ -NP/FAU. This means that, although extra-layers of  $\text{Ce}_{0.9}\text{Zr}_{0.1}\text{O}_2$ -NP are dispersed on the FAU surface, the soot-catalyst contact points play the main role in

**Table 4**  
Soot oxidation activity results, under “loose” contact conditions of the prepared materials.

Catalyst	$T_{10\%}$ (°C)	$T_{50\%}$ (°C)	$T_{90\%}$ (°C)
$\text{Ce}_{0.9}\text{Zr}_{0.1}\text{O}_2$ -NP	427	491	540
$\text{Ce}_{0.8}\text{Zr}_{0.2}\text{O}_2$ -NP	449	526	585
$\text{Ce}_{0.7}\text{Zr}_{0.3}\text{O}_2$ -NP	493	580	631
25- $\text{Ce}_{0.9}\text{Zr}_{0.1}\text{O}_2$ -NP/FAU	527	607	652
50- $\text{Ce}_{0.9}\text{Zr}_{0.1}\text{O}_2$ -NP/FAU	444	537	604
75- $\text{Ce}_{0.9}\text{Zr}_{0.1}\text{O}_2$ -NP/FAU	477	537	604
$\text{Ce}_{0.9}\text{Zr}_{0.1}\text{O}_2$ -M	460	531	582
$\text{Ce}_{0.9}\text{Zr}_{0.1}\text{O}_2$ -SCS	495	590	634
FAU-type zeolite	544	621	665
Printex-U	540	620	665

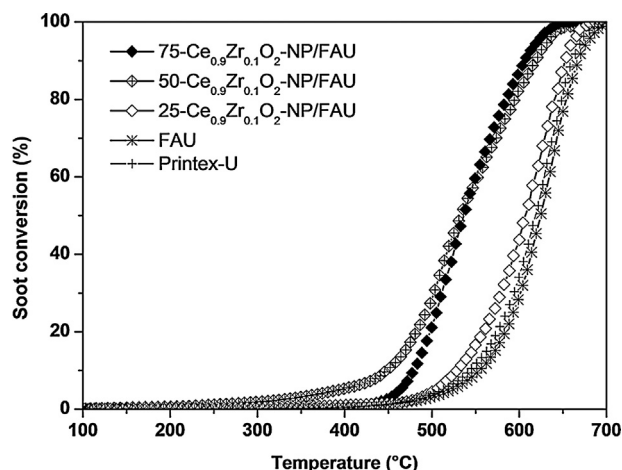


**Fig. 10.** Soot conversion (%), as a function of temperature, over the 25-, 50-, and 75-Ce<sub>0.9</sub>Zr<sub>0.1</sub>O<sub>2</sub>-NP/FAU catalysts, FAU-type zeolite and Printex-U (no catalyst) using “loose” soot-catalyst conditions.

this solid–solid–gas system. On the other hand, better results, in terms of the onset of soot oxidation, have been reached for the 50-Ce<sub>0.9</sub>Zr<sub>0.1</sub>O<sub>2</sub>-NP/FAU catalyst, thus, reflecting the beneficial role of surface area (hence sorbed active oxygens) at low temperatures (see  $T_{10\%}$  in Table 1). The worst performances were achieved for the 25-Ce<sub>0.9</sub>Zr<sub>0.1</sub>O<sub>2</sub>-NP/FAU catalyst, as a consequence of the very low amount of active phase dispersed over the support.

According to the literature, ceria–zirconia materials should be more reactive than pure ceria [4,16,65–68]. However, the structural parameters of nanocatalysts play a key role in oxidation catalysis, and hence a proper comparison of the surface reactivity is often difficult to accomplish, due to the complexity of nanocatalysts. Fig. 11A shows superior activities (in terms of  $T_{90\%}$ ) for Ce<sub>0.9</sub>Zr<sub>0.1</sub>O<sub>2</sub>-NP than those reported for CeO<sub>2</sub> nanoparticles, in “loose” contact (denoted as “Ce-NC” in Ref. [31]). It therefore seems that the redox properties of ceria–zirconia materials are enhanced at high temperatures, with respect to CeO<sub>2</sub>-NC, and hence a higher mobility of lattice oxygen within the solid can be expected (*vide supra*). However, at low temperatures, the activity of the Ce<sub>0.9</sub>Zr<sub>0.1</sub>O<sub>2</sub>-NP is comparable with that of Ce-NC (e.g., in terms of  $T_{10\%}$  and  $T_{50\%}$ ), although dissimilar soot conversion trends appear, likely due to the different physico-chemical properties. Moreover, different multimodal distributions of CO<sub>2</sub> and CO formation have been obtained for the two materials (Fig. 11B and C, respectively), thus, confirming the presence of various surface reactivities (and hence catalytic behavior) over the whole temperature range. In particular, Ce<sub>0.9</sub>Zr<sub>0.1</sub>O<sub>2</sub>-NP shows a uniform distribution of the CO<sub>2</sub> concentration, centered at ca. 490°C, thus, suggesting the presence of similar reactivities for the exposed surfaces. Equiv-

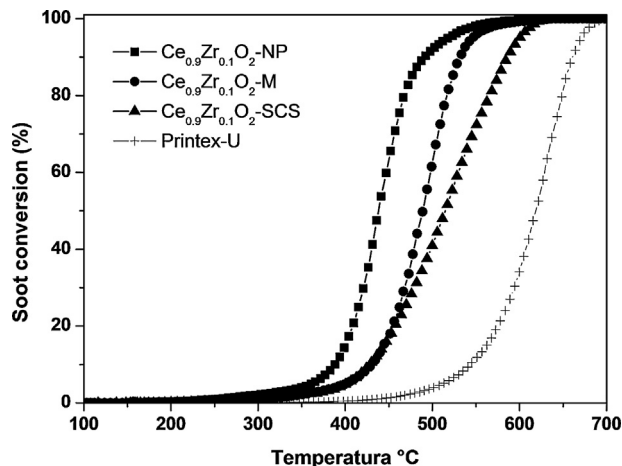


**Fig. 12.** Soot conversion (%), as a function of temperature, over the ceria-zirconia catalysts, FAU-type zeolite and Printex-U (no catalyst) using “tight” soot-catalyst conditions.

alent results were observed for the other ceria–zirconia catalysts (not reported for the sake of brevity).

The catalytic activity of the three ceria–zirconia samples with the same Ce/Zr ratio (Ce<sub>0.9</sub>Zr<sub>0.1</sub>O<sub>2</sub>-NP, Ce<sub>0.9</sub>Zr<sub>0.1</sub>O<sub>2</sub>-M, and Ce<sub>0.9</sub>Zr<sub>0.1</sub>O<sub>2</sub>-SCS) has also been tested under “tight” contact conditions, in order to better discriminate between the different structures [69] (Fig. 12). As expected, an improvement in the activities was achieved for all the prepared catalysts, with respect to loose-conditions, and the following catalytic activity scale can be drawn: Ce<sub>0.9</sub>Zr<sub>0.1</sub>O<sub>2</sub>-NP > Ce<sub>0.9</sub>Zr<sub>0.1</sub>O<sub>2</sub>-M > Ce<sub>0.9</sub>Zr<sub>0.1</sub>O<sub>2</sub>-SCS. Moreover, the soot conversion curves rapidly increase for the three catalysts, as a function of temperature, as a consequence of the more effective soot-catalyst interactions (=effective mass transport phenomena).

In order to analyze the stability of the catalysts, three successive runs were performed under “tight” contact conditions [69]. Fig. 13A shows the catalytic performances of the most active catalyst (Ce<sub>0.9</sub>Zr<sub>0.1</sub>O<sub>2</sub>-NP), as a function of temperature, for each heating run kept at 700°C for 2 h. As a result, similar performances were achieved during three catalytic cycles, and no deactivation was observed in terms of soot conversion values, thus confirming the good stability of the material. Comparable results, in terms of catalytic stability, were achieved for Ce<sub>0.9</sub>Zr<sub>0.1</sub>O<sub>2</sub>-M (Fig. 13B) and Ce<sub>0.9</sub>Zr<sub>0.1</sub>O<sub>2</sub>-SCS (Fig. 13C).

The reproducibility of the catalytic results has been studied by carrying out tests in “loose” contact conditions, in order to simulate the real conditions that occur in a catalytic trap. As a whole, a good test-retest reproducibility of the catalytic performances was achieved with the prepared ceria–zirconia catalysts, and the maxi-

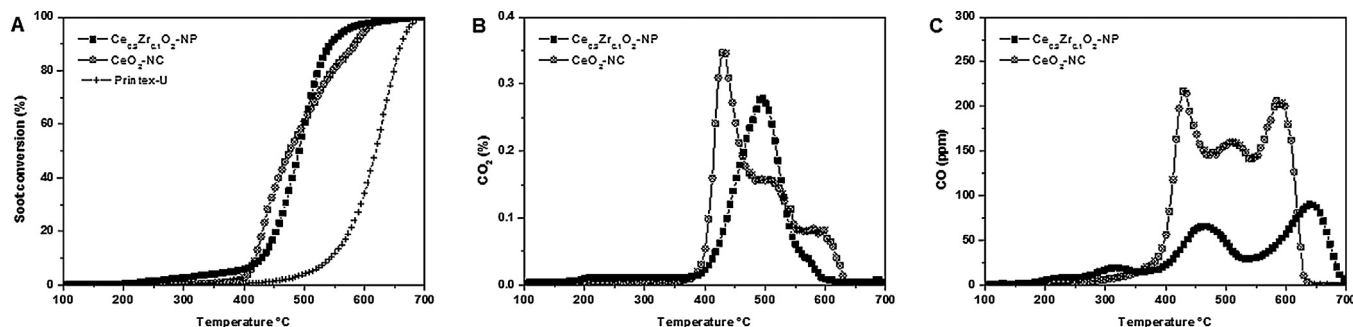


**Fig. 11.** Soot conversion (%) (Section A), CO<sub>2</sub> concentration (%) (Section B), and CO concentration (ppm) (Section C), as a function of temperature, over Ce<sub>0.9</sub>Zr<sub>0.1</sub>O<sub>2</sub>-NP and CeO<sub>2</sub> (Ce-NC, reported in Ref. [31]) using “loose” soot-catalyst conditions.

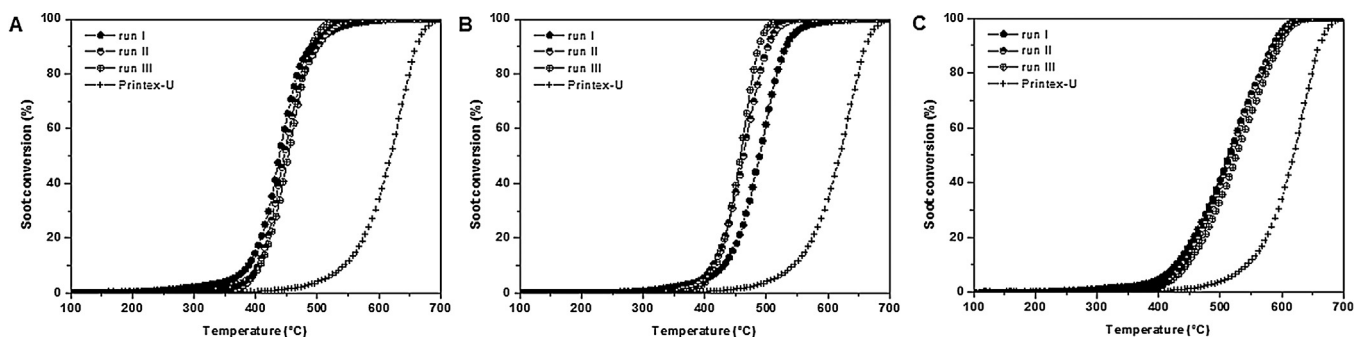


**Fig. 13.** Stability study of the catalytic performances of the  $\text{Ce}_{0.9}\text{Zr}_{0.1}\text{O}_2\text{-NP}$  (Section A),  $\text{Ce}_{0.9}\text{Zr}_{0.1}\text{O}_2\text{-M}$  (Section B), and  $\text{Ce}_{0.9}\text{Zr}_{0.1}\text{O}_2\text{-SCS}$  (Section C) catalyst for three successive catalytic cycles using “tight” soot-catalyst contact conditions.

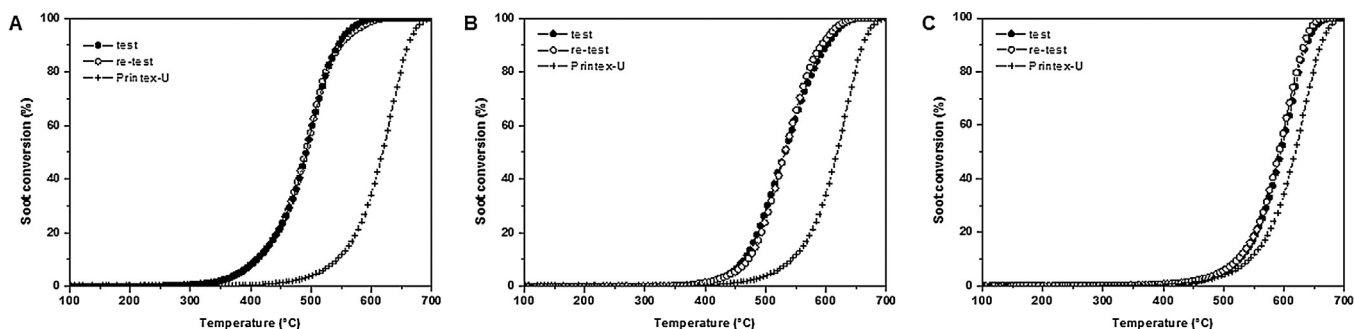


**Fig. 14.** Test-retest reproducibility of the catalytic performances of  $\text{Ce}_{0.9}\text{Zr}_{0.1}\text{O}_2\text{-NP}$  (Section A),  $\text{Ce}_{0.9}\text{Zr}_{0.1}\text{O}_2\text{-M}$  (Section B), and  $\text{Ce}_{0.9}\text{Zr}_{0.1}\text{O}_2\text{-SCS}$  (Section C) using “loose” contact conditions.

imum deviation from the mean conversion value over repeated tests was  $\pm 5^\circ\text{C}$  (Fig. 14). This means that such ceria–zirconia materials should be considered valuable candidates for catalytic applications in DPFs. Nevertheless, further kinetic modelling will be necessary to better understand the catalytic behavior of these mixed oxide catalysts, as well as the catalyst–soot contact conditions have to be fully understood in order to develop effective catalytic traps.

#### 4. Conclusions

A set of ceria–zirconia catalysts with different Zr-contents and structural properties has been prepared to study both the effect of the Zr-amount and the surface-dependency activity of catalysts towards soot combustion, both in “loose” and “tight” contact conditions. As a whole, the best catalytic results (in terms of  $T_{10\%}$ ,  $T_{50\%}$ , and  $T_{90\%}$ ) have been achieved for the  $\text{Ce}_{0.9}\text{Zr}_{0.1}\text{O}_2\text{-NP}$  catalyst, due to the higher mobility of lattice oxygen within the solid and its easier reducibility, rather than for high-surface area catalysts with the same Ce/Ce + Zr ratio. Moreover, better catalytic activities have been pointed out for the  $\text{Ce}_{0.9}\text{Zr}_{0.1}\text{O}_2\text{-NP}$  catalyst, compared to nano-polyhedra with higher Zr-contents (namely  $\text{Ce}_{0.8}\text{Zr}_{0.2}\text{O}_2\text{-NP}$  and  $\text{Ce}_{0.7}\text{Zr}_{0.3}\text{O}_2\text{-NP}$ ).

The substitution of some  $\text{Ce}^{4+}$  for  $\text{Zr}^{4+}$  ions favours the formation of defects (i.e., oxygen vacancies) in the ceria–zirconia lattice, and thus induces the distortion of the oxygen sublattice. However, the surface density of an active redox element (cerium) decreases as the Zr-content increases. It therefore, seems that the incorporation of  $\text{Zr}^{4+}$  into the ceria lattice does not have a direct beneficial effect on soot oxidation for catalysts calcined at low/mild temperature (namely, below  $600^\circ\text{C}$ ), since it decreases the population of surface redox-active centres, which are directly dependent on the surface density of the  $\text{Ce}^{3+}\text{-Ce}^{4+}$  species. Lower soot conversion values have been obtained for both  $\text{Ce}_{0.9}\text{Zr}_{0.1}\text{O}_2\text{-M}$  and  $50\text{-Ce}_{0.9}\text{Zr}_{0.1}\text{O}_2\text{-NP/FAU}$  samples with the same Ce/Zr ratio. Moreover, the comparative catalyst ( $\text{Ce}_{0.9}\text{Zr}_{0.1}\text{O}_2\text{-SCS}$ ) exhibited worse

activities than the meso-microporous materials, thus, confirming the key role of the textural properties on this oxidation reaction. Thus, the following catalytic activity scale has been proposed:  $\text{Ce}_{0.9}\text{Zr}_{0.1}\text{O}_2\text{-NP} > \text{Ce}_{0.9}\text{Zr}_{0.1}\text{O}_2\text{-M} > \text{Ce}_{0.9}\text{Zr}_{0.1}\text{O}_2\text{-SCS}$ .

Finally, the stability of the catalysts, as well as the reproducibility of the catalytic results, has been confirmed through multiple tests.

#### Acknowledgments

The Ministero dell'Università e della Ricerca (MIUR) (grant number: RBFR12LS6M 001) is acknowledged for sponsoring this research activity (FIRB – Futuro in Ricerca 2012). Authors thank Prof. Fabrizio Giorgis and Dr. Alessandro Virga (Politecnico di Torino, Italy) for Raman measurements. Moreover, the authors are very grateful to the reviewer's valuable comments that improved the manuscript.

#### References

- [1] A. Trovarelli, P. Fornasiero, *Catalysis by Ceria and Related Materials*, 2nd ed., Imperial College Press, London, 2013, pp. 565–621.
- [2] R.M. Heck, R.J. Farrauto, S.T. Gulati, *Catalytic Air Pollution Control: Commercial Technology*, 3rd ed., Wiley-VCH, Hoboken, New Jersey, 2006, pp. 1–518.
- [3] G. Ertl, H. Knözinger, F. Schüth, J. Weitkamp, *Handbook of Heterogeneous Catalysis*, 2nd ed., Wiley-VCH, Weinheim, 2008, pp. 2274–2344.
- [4] A. Bueno-López, *Appl. Catal. B* 146 (2014) 1–11.
- [5] R. Burch, *Catal. Rev.* 46 (2004) 233–271.
- [6] A. Russell, W.S. Epling, *Catal. Rev. Sci. Eng.* 53 (2011) 337–423.
- [7] P. Eastwood, *Critical Topics in Exhaust Gas Aftertreatment*, Research Studies Press Ltd., Baldock, England, 2000, pp. 400.
- [8] J. Oi-Uchisawa, A. Obuchi, S. Wang, T. Nanba, A. Ohi, *Appl. Catal. B* 43 (2003) 117–129.
- [9] C.A. Neyertz, E.D. Banus, E.E. Miró, C.A. Querini, *Chem. Eng. J.* 248 (2014) 394–405.
- [10] E. Aneggi, D. Wiater, C. de Leitenburg, J. Llorca, A. Trovarelli, *ACS Catal.* 4 (2014) 172–181.

- [11] I. Atribak, F.E. Lopez-Suarez, A. Bueno-Lopez, A. Garcia-Garcia, *Catal. Today* 176 (2011) 404–408.
- [12] M. Issa, C. Petit, A. Brillard, J.-F. Brilhac, *Fuel* 87 (2008) 740–750.
- [13] E. Aneggi, C. de Leitenburg, A. Trovarelli, *Catal. Today* 181 (2012) 108–115.
- [14] S. Bensaid, N. Russo, D. Fino, *Catal. Today* 216 (2013) 57–63.
- [15] P.A. Kumar, M.D. Tanwar, S. Bensaid, N. Russo, D. Fino, *Chem. Eng. J.* 207–208 (2012) 258–266.
- [16] E. Aneggi, M. Boaro, C. de Leitenburg, G. Dolcetti, A. Trovarelli, *J. Alloy Comp.* 408–412 (2006) 1096–1102.
- [17] G. Pacchioni, *ChemPhysChem* 4 (2003) 1041–1047.
- [18] K. An, G.A. Somorjai, *Catal. Lett.* 145 (2015) 233–248.
- [19] F. Volkenshtein, *The Electronic Theory of Catalysis on Semiconductors*, Pergamon Press, New York, 1963.
- [20] R.A. van Santen, M. Neurock, *Molecular Heterogeneous Catalysis*, Wiley-VCH, Verlag, 2006, pp. 474.
- [21] G.A. Somorjai, *Langmuir* 7 (1991) 3176–3182.
- [22] G.A. Somorjai, J.Y. Park, *Catal. Lett.* 115 (2007) 87–98.
- [23] S. Chowdhury, K.-S. Lin, J. Nanomater. 2011 (2011) 1–16.
- [24] W.Q. Han, W. Wen, J.C. Hanson, X.W. Teng, N. Marinkovic, J.A. Rodriguez, *J. Phys. Chem. C* 113 (2009) 21949–21955.
- [25] N. Ta, J. Liu, S. Chenna, P.A. Crozier, Y. Li, A. Chen, W.J. Shen, *J. Am. Chem. Soc.* 134 (2012) 20585–20588.
- [26] C.S. Pan, D.S. Zhang, L.Y. Shi, J.H. Fang, *Eur. J. Inorg. Chem.* 15 (2008) 2429–2436.
- [27] Z.L. Wu, M.J. Li, S.H. Overbury, *J. Catal.* 285 (2012) 61–73.
- [28] N.K. Renuka, A.K. Praveen, C.U. Aniz, *Micropor. Mesopor. Mater.* 169 (2013) 35–41.
- [29] X. Du, D. Zhang, L. Shi, R. Gao, J. Zhang, *J. Phys. Chem. C* 116 (2012) 10009–10016.
- [30] W.I. Hsiao, Y.S. Lin, Y.C. Chen, C.S. Lee, *Chem. Phys. Lett.* 441 (2007) 294–299.
- [31] M. Piumetti, S. Bensaid, N. Russo, D. Fino, *Appl. Catal. B* 165 (2015) 742–751.
- [32] K.B. Zhou, X. Wang, X.M. Sun, Q. Peng, Y.D. Li, *J. Catal.* 229 (2005) 206–212.
- [33] Z.X. Yang, T.K. Woo, M. Baudin, K. Hermansson, *J. Chem. Phys.* 120 (2004) 7741–7749.
- [34] T.X.T. Sayle, M. Cantoni, U.M. Bhatta, S.C. Parker, S.R. Hall, G. Mobus, M. Molinari, D. Reid, S. Seal, D.C. Sayle, *Comm. Mater.* 24 (2012) 1811–1821.
- [35] J. Zhang, H. Kumagai, K. Yamamura, S. Ohara, S. Takami, A. Morikawa, H. Shinjoh, K. Kaneko, T. Adschiri, A. Suda, *Nano Lett.* 11 (2011) 361–364.
- [36] M. Hirano, K. Hirai, *J. Nanopart. Res.* 5 (2003) 147–156.
- [37] A. Civera, M. Pavese, G. Saracco, V. Specchia, *Catal. Today* 83 (2003) 199–211.
- [38] E. Aneggi, C. de Leitenburg, G. Dolcetti, A. Trovarelli, *Catal. Today* 114 (2006) 40–47.
- [39] V. Sánchez Escribano, E.F. López, M. Panizza, C. Resini, J.M. Gallardo Amores, G. Busca, *Solid State Sci.* 5 (2003) 1369–1376.
- [40] B.D. Cullity, S.R. Stock, *Elements of X-Ray Diffraction*, 3rd ed., Prentice-Hall Inc., 2001, 2015, pp. 167–171.
- [41] Database of Zeolite Structures, <http://www.iza-structure.org/>
- [42] M. Hussain, N. Russo, G. Saracco, *Chem. Eng. J.* 166 (2011) 138–149.
- [43] A. Savara, A. Danon, W.M.H. Sachtler, E. Weitz, *Phys. Chem. Chem. Phys.* 11 (2009) 1180–1188.
- [44] P. Ji, J. Zhang, F. Chen, M. Anpo, *J. Phys. Chem. C* 112 (2008) 17809–17813.
- [45] B. Puertolas, B. Solsona, S. Agouram, R. Murillo, A.M. Mastral, A. Aranda, S.H. Taylor, T. Garcia, *Appl. Catal. B* 93 (2010) 395–405.
- [46] Agarwal, L. Lefferts, B.L. Mojet, *ChemCatChem* 5 (2013) 479–489.
- [47] G. Wulff, *Z. Kristallogr. Mineral* 34 (1901) 449–530.
- [48] J.M. Gatica, D.M. Gómez, J.C. Hernández-Garrido, J.J. Calvino, G.A. Cifredo, H. Vidal, *Appl. Catal. A* 479 (2014) 35–44.
- [49] B. Bulfin, A.J. Lowe, K.A. Keogh, B.E. Murphy, O. Lübben, S.A. Krasnikov, I.V. Shvets, *J. Phys. Chem. C* 117 (46) (2013) 24129–24137.
- [50] G. Zhang, Z. Shen, M. Liu, C. Guo, P. Sun, Z. Yuan, B. Li, D. Ding, T. Chen, *J. Phys. Chem. B* 110 (2006) 25782–25790.
- [51] B.M. Reddy, A. Khan, Y. Yamada, T. Kobayashi, S. Lorient, J.-C. Volta, *J. Phys. Chem. B* 107 (2003) 5162–5167.
- [52] G.I. Golodets, In: G. Centi, F. Trifirò (Eds.) *Stud. Surf. Sci. Catal. New Developments in Selective Oxidation* 55 (1990) 693.
- [53] A. Bueno-López, K. Krishna, M. Makkee, J.A. Moulijn, *J. Catal.* 230 (2005) 237–248.
- [54] A. Galtayries, R. Sporken, J. Riga, G. Blanchard, R. Caudano, *J. Electr. Spectrosc. Rel. Phenomena* 88–91 (1998) 951–956.
- [55] P.C. Wong, Y.S. Li, K.A.R. Mitchell, *Surf. Rev. Lett.* 2 (3) (1995) 297–303.
- [56] S. Suhonen, M. Valden, M. Hietikko, R. Laitinen, A. Savimäki, M. Härkönen, *Appl. Catal. A* 218 (2001) 151–160.
- [57] O.H. Laguna, M.A. Centeno, F. Romero-Sarria, J.A. Odriozola, *Catal. Today* 172 (2011) 118–123.
- [58] L.F. Nascimento, R.F. Martins, R.F. Silva, P.C. de Sousa Filho, O.A. Serra, *Reac. Kinet. Mech. Catal.* 111 (2014) 149–165.
- [59] W.Y. Hernandez, M.A. Centeno, F. Romero-Sarria, J.A. Odriozola, *J. Phys. Chem. C* 113 (2009) 5629–5635.
- [60] E. Aneggi, C. de Leitenburg, J. Llorca, A. Trovarelli, *Catal. Today* 197 (2012) 119–126.
- [61] K. Krishna, A. Bueno-López, M. Makkee, J.A. Moulijn, *Appl. Catal. B* 75 (2007) 191–202.
- [62] K. Krishna, A. Bueno-López, M. Makkee, J.A. Moulijn, *Appl. Catal. B* 75 (2007) 203–211.
- [63] K. Krishna, A. Bueno-López, M. Makkee, J.A. Moulijn, *Appl. Catal. B* 75 (2007) 212–222.
- [64] K.W. Kolasinski, *Surface Science*, 3rd ed., Wiley-VCH, Verlag, 2012, pp. 553.
- [65] I. Atribak, B. Azambre, A. Bueno López, A. García-García, *Appl. Catal. B* 92 (2009) 126–137.
- [66] I. Atribak, A. Bueno-López, A. Garcia, *Catal. Comm.* 9 (2008) 250–255.
- [67] B.K. Hodnett, *Heterogeneous Catalytic Oxidation*, Wiley-VCH, New York, 2000, pp. 347.
- [68] Q. Liang, X. Wu, X. Wu, D. Weng, *Catal. Lett.* 119 (2007) 265–270.
- [69] J.P.A. Neeft, M. Makkee, J.A. Moulijn, *Appl. Catal. B* 8 (1996) 57–78.